SCIENCE CHINA
Information Sciences

• **Supplementary File** •

High-performance Carbon-electrode-based Self-powered Optoelectronic Synaptic Devices

Wen Huang[1], Xuwen Xia[1], Huixing Zhang[1], Tenglong Guo[3], Pengjie Hang[2*], Bin Li[1], Jiawei Tang[1], Biao Li[2], Chen Zhu[3], Lei Wang[3], Deren Yang[2], Xuegong Yu[2*] & Xing'ao Li[1*]

[1]*Jiangsu Provincial Engineering Research Center of Low Dimensional Physics and New Energy & School of Science, Nanjing University of Posts and Telecommunications, Nanjing* 210023*, China;*
[2]*State Key Laboratory of Silicon and Advanced Semiconductor Materials, Zhejiang University, Hangzhou* 310027*, China;*
[3]*College of Integrated Circuit Science and Engineering, Nanjing University of Posts and Telecommunications, Nanjing* 210023*, China*

Appendix A Device fabrication and characterization details

Material preparation: Titanium (IV) isopropoxide, isopropanol, N,N-dimethylformamide (DMF), and dimethyl sulfoxide (DMSO) were purchased from Sigma-Aldrich. Hydrochloride (HCl) was bought from Sinopharm Chemical Reagent Co., Ltd. Ethanol was purchased from Shanghai Macklin Biochemical Co., Ltd. MAI, PbI_2, Spiro-OMeTAD, and Dyesol 18NRT (TiO_2 paste) were purchased from Xi'an Polymer Light Technology Corp. FTO coated on glass was from Hangzhou Hongshi Electronic Technology Co., Ltd. Four FTO strips with 500 μm wide for each one were obtained through a mask when using a magnetic sputtering technique. Conductive carbon ink was purchased from Shanghai Mater Win New Materials Co., Ltd.

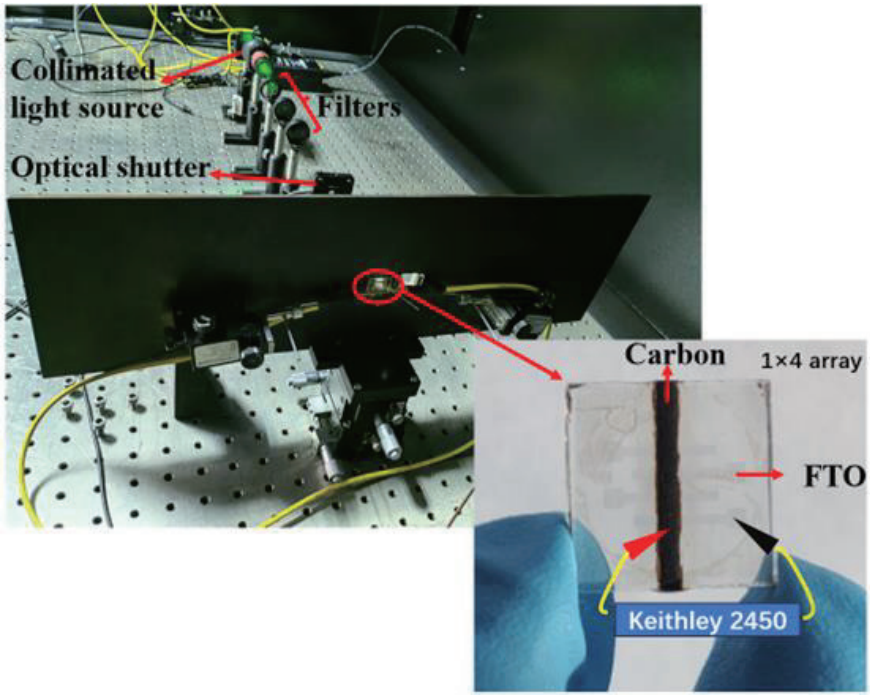

Figure A1 Photograph of the measurement setup and the device.

Device fabrication: The constructed device array features a 1×4 crossbar design with carbon and FTO strips and is 1000 μm × 500 μm in size for each device. The patterned FTO glasses underwent a cleansing with deionized water, acetone, and ethanol for 15 min each. Subsequently, the glasses were dried and then subjected to a 15-min UV-ozone treatment to establish the desired wettability surface. To create the compact TiO_2 (C-TiO_2) layer, we spin-coated a TiO_2 organic solution onto the FTO-coated glass substrates at a speed of 2500 rpm for 30 s. This was followed by a drying process at 260 °C (380 °C, 500 °C) for 30 min.

* Corresponding author (email: hangpengjie@zju.edu.cn, yuxuegong@zju.edu.cn, lixa@njupt.edu.cn)

The organic solution used for this purpose consisted of 370 μL titanium (IV) isopropoxide, 2.53 ml isopropanol, and 35 μl HCl solution. The mesoporous TiO_2 (M-TiO_2) layer was prepared using commercial TiO_2 paste Dyesol 18NRT, which was diluted in ethanol at a weight ratio of 1:7. This mixture was applied via spin-coating, first at 1000 rpm for 5 s and then at 5000 rpm for 25 s. Next, gradual heating was employed to raise the temperature to 260 °C (380 °C,500 °C), and the layer was finally baked at this temperature for 30 min. To create the perovskite precursor solution, we dissolved 461 mg of PbI_2 and 159 mg of MAI in 630 μL of DMF solution. Following this, we added 71 μL of DMSO to the DMF solution to prepare the optically active layer $MAPbI_3$ for the device. The fabrication of this layer involved a one-step deposition method, where it was spin-coated at 4000 rpm for 20 s, baked at 75 °C for 10 min, and subsequently at 105 °C for an additional 10 min. Finally, a 1000 μm-wide carbon strip was applied on top of the $MAPbI_3$ film using a doctor blade coating process with carbon ink, and then dried at 100 °C for 20 min.

Device characterization: The detailed synaptic characterization setup and device array information can be seen in Figure A1. The filters are used for adjusting the light source intensity.

Appendix B Device characteristics

The carbon layer as the electrode of the device is demonstrated in Figure B1(a). It was prepared with conductive carbon ink as seen in the bottle, and the X-ray diffraction (XRD) pattern of the carbon film is shown in Figure B1(b). The narrow peaks (002) and (004) were obtained from the flaky graphite of the carbon film [1]. To demonstrate the role of carbon in the device, the inset of Figure B1(b) shows the photoluminescence (PL) property of $MAPbI_3$ films in the device, which demonstrated that it had a stronger PL (796 nm) property of $MAPbI_3$ films than that of $MAPbI_3$ films with carbon electrodes. This result proved that the carbon electrode may extract holes and can function as a hole acceptor as well [2]. Figure 1b demonstrates a cross-sectional SEM image of the FTO/C-TiO_2/M-TiO_2/$MAPbI_3$/carbon device. The C-TiO_2 exhibited an approximate thickness of 80 nm, while the M-TiO_2 film was about 290 nm thick. The $MAPbI_3$ may partially infiltrate the pores within the M-TiO_2 film [1]. Moreover, a large $MAPbI_3$ crystal approximately 350 nm in size was observed on top of the TiO_2 film. A hysteresis phenomenon was discovered when consecutive bias sweeps (−1.0 V to 1.0 V) were applied to the device (see Figure B1(c), serving as evidence of the device's memristive characteristics. Notably, the amplitude of the dark current exhibited a gradual increment in the forward region, reaching a stable loop as it increased to 10 times. This change is illustrated by the current-voltage ($I-V$) curves. Figure B1(d) shows that the optical spectra of both $MAPbI_3$ (380 nm − 800 nm) and TiO_2 films (325 nm − 800 nm). These spectra clearly showcase the outstanding optical absorption of $MAPbI_3$ films and optical transmission of TiO_2 films, within the visible light spectrum. Finite difference time-domain simulation was used to demonstrate the optical absorption distribution of the device as shown in Figure B1(e). This is consistent with the corresponding optical properties of $MAPbI_3$ and TiO_2 films. These findings underscore the high potential of the hybrid structure based on TiO_2/$MAPbI_3$ heterojunction in optoelectronic synaptic devices.

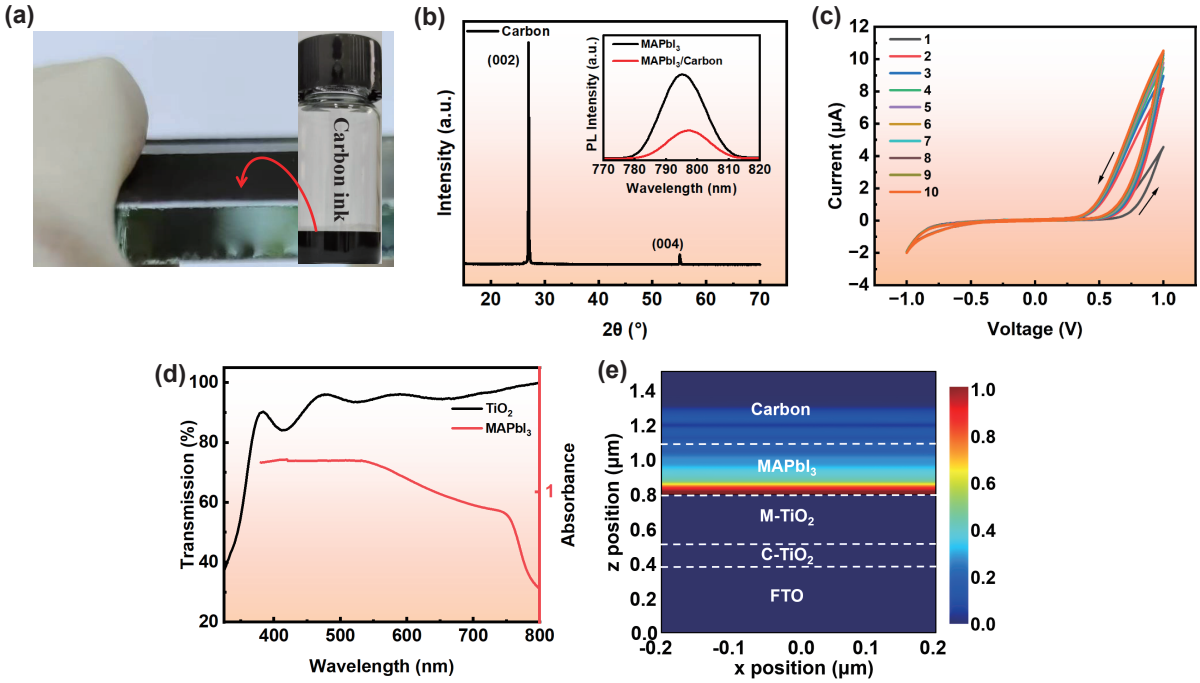

Figure B1 (a) Schematics of a carbon layer used for the electrode and the synthetic raw materials of carbon ink.(b) Schematics of an X-ray diffraction pattern of the carbon film and the PL property of $MAPbI_3$.(c) $I-V$ curves of the device.(d) Optical absorption of $MAPbI_3$ and transmission of TiO_2 films.(e)Finite-difference time-domain simulation for optical absorption

The energy band structure of TiO_2 annealed at 260 °C was investigated by combining ultraviolet photoelectron spectroscopy (UPS) and optical absorption spectroscopy [3]. The energy band structure information in the structure was then extracted based on the measurement results (Figure B2(a) and Figure B2(b) and the reference [4]. The heterojunction band diagram of the device was therefore dictated as shown in Figure 1d, which clearly reveals that the photogenerated electrons and holes in the perovskite can inject efficiently into TiO_2 and carbon electrode with the built-in electric field, respectively. This illustrates that the photocurrents are then formed based on the photovoltaic effects. No external bias voltage is then needed for the carrier transport in the device, indicating the zero electrical energy consumption for driving the carrier transport in mimicking synaptic functions [5].

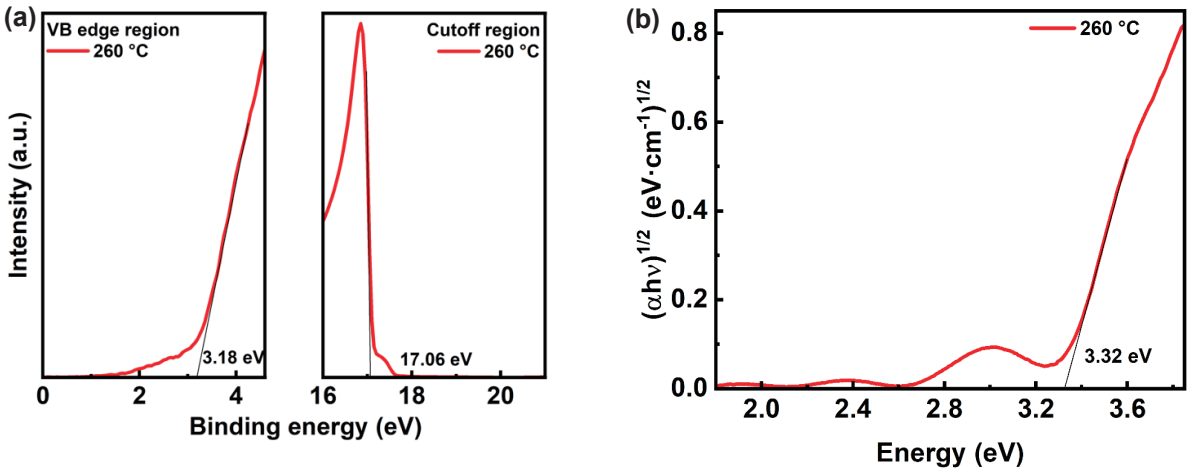

Figure B2 (a) A schematic of UPS characterization for the TiO_2 film.(b) A schematic diagram of Tauc plot.

Appendix C Mimicking of synaptic functions

The alterations in EPSC in response to changes in optical pulse power and width are illustrated in Figures C1(a) and C1(b). As both pulse power and width increased, the current increased correspondingly. The current reached a level of 840 pA for a single pulse power density of ∼3119 $\mu W/cm^2$ and about 323 pA for a pulse width of 2 s. The initiation of synaptic current can be achieved via a pair of optical pulses, each with a pulse duration of 0.05 s. These pulses occur at varying time intervals (Δt = 0.05 s to 4 s). Note that the current (C2) initiated by the second optical pulse is larger than the current (C1) initiated by the first pulse, which is a phenomenon identified as PPF [6]. The computed PPF index (C2:C1) exhibited an exponential decay pattern with the progressive increment of Δt (see inset of Figure S(3c)). Rapid (0.02 s) and slow (0.7 s) decay parameters were estimated by fitting the well-known double-exponential decay function to the PPF indexes as illustrated in the inset of Figure C1(c).

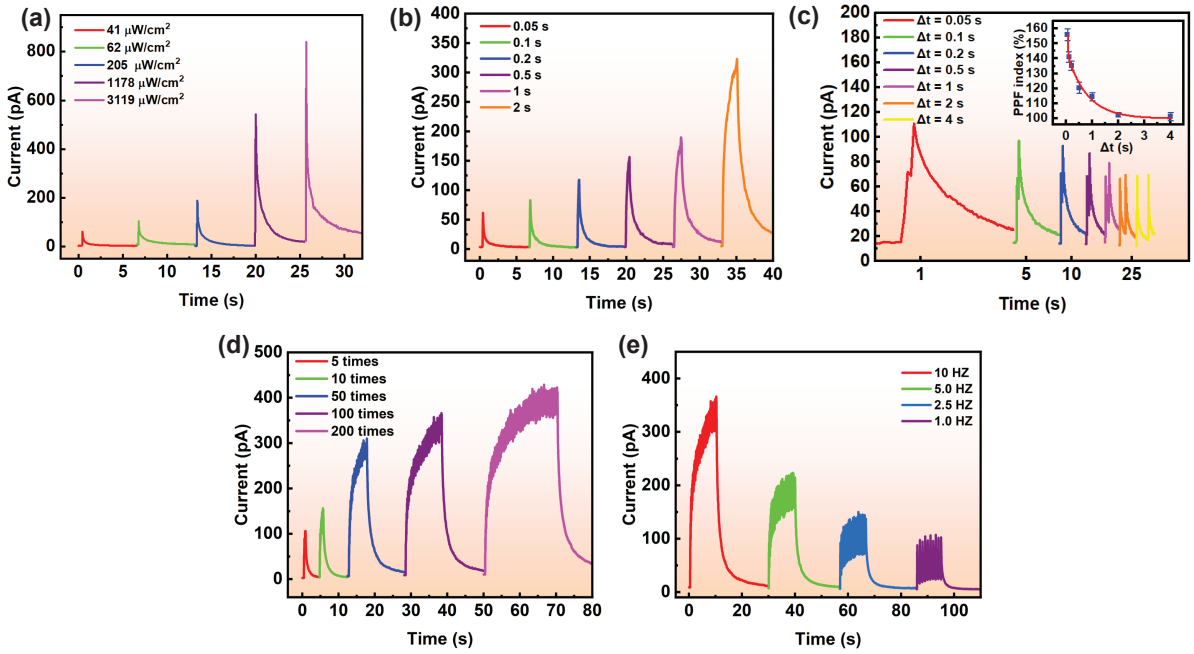

Figure C1 (a) Relationship between EPSC response and various optical power densities. (b) Relationship between EPSC response and various optical pulse widths. (c) Schematics depicting the behaviors of PPF and their corresponding indexes. (d) Relationship between EPSC response and various optical pulse numbers. (e) Relationship between EPSC response and various optical pulse frequencies.

The synaptic currents of the device in response to 5, 10, 50, 100, and 200 optical pulses are shown in Figure C1(d). The synaptic currents demonstrated an increasing trend, ranging from approximately 106 pA to about 423 pA, with variations in the number of optical pulses from 5 to 200. At the same time, the decay time increased from approximately 2 s to around 7 s as the number of optical pulses rose. These observed behaviors effectively demonstrate the mimicking of SNDP synaptic functions in synaptic devices. Figure C1(e) shows that in response to consecutive optical pulse stimulation, the synaptic currents increased from about 102 pA to approximately 366 pA, corresponding to the rise of optical pulse frequency from 1 Hz to 10 Hz. Simultaneously, the decay

time for these synaptic currents increased to approximately 5.4 s from around 2.8 s. These results affirm the successful mimicking of SRDP synaptic functions. These observed functions, including EPSC, PPF, SNDP, and SRDP, closely align with the synaptic behaviors exhibited by biological synapses within neural systems [7–9].

Appendix D Work mechanism analysis

Figure 1c shows the EPSC response of the device. This synaptic current was generated without an external bias supply in response to an optical pulse at the wavelength of 532 nm. The optical power density was ∼41 μW/cm^2, with a pulse width of 0.05 s. During this optical stimulation, the current reached the maximum value of 65 pA. After the removal of optical pulses, the decay time was found to be ∼1.68 s based on the current change from 90% to 10% of the original value. It was verified that one of the most dominant defects observed in TiO_2 film is oxygen vacancies [10], which give rise to the local states below the conduction band edge (Figure 1d). These states may trap some electrons from the perovskite and then release them slowly, leading to slow decay behaviors of the photocurrents in the device and thereby successfully mimicking the synaptic functions. There is no current response for the TiO_2 layer to the 532 nm stimulation in this structure, which can be clearly reflected with the blue line in Figure 1c. This indicates that the photo-generated carriers that contribute to synaptic current response is mainly arising from the perovskite instead of TiO_2.

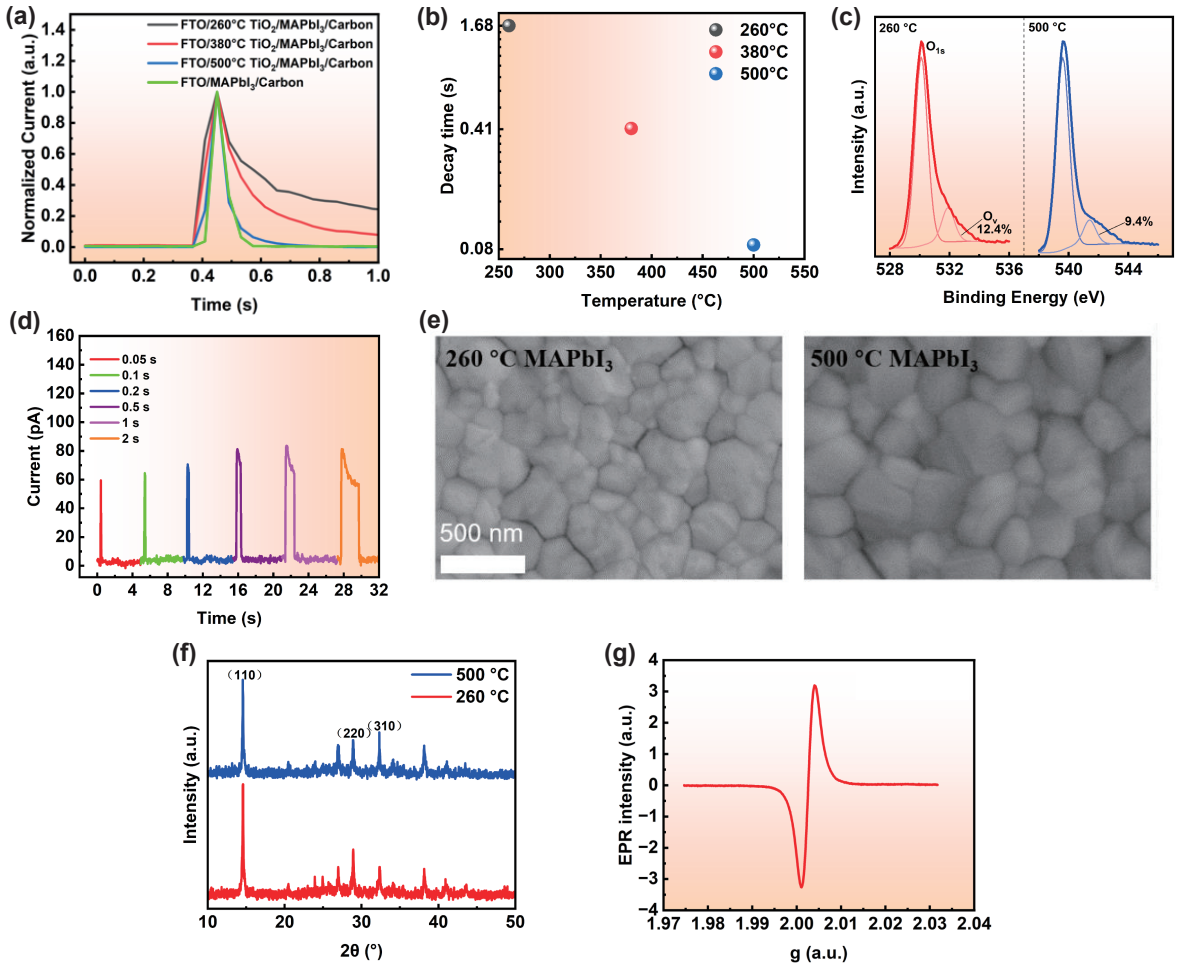

Figure D1 (a) Normalized EPSC results of TiO_2 films at different annealing temperatures. (b) The decay change of the EPSC for TiO_2 films at different annealing temperatures. (c) The XPS characterization for TiO_2 films at annealing temperatures of 260 °C and 500 °C. (d) Photocurrent current response of the $MAPbI_3$ film-based device (TiO_2 free). (e) The SEM characterization for $MAPbI_3$ films for TiO_2-free and TiO_2 layers at annealing temperatures of 260 °C and 500 °C.(f) The XRD patterns for $MAPbI_3$ films on different annealing-temperature.(g) The EPR measurement of the TiO_2 layer.

Moreover, the normalized photocurrents of the devices at different annealing temperatures (260°C, 380 °C, and 500 °C) for TiO_2 films were compared and the decay time was found to decrease from ∼1.68 s to ∼0.08 s versus the increase of temperatures (Figure D1(a) and Figure D1(b)). Oxygen vacancy concentration was found to decrease from 12.4% at annealing temperature of 260 °C to 9% at annealing temperature of 500 °C for TiO_2 films (Figure D1(c)), while no obvious difference was observed for the perovskite crystallization situation based on SEM and XRD patterns of perovskites on top of TiO_2 films at these two annealing temperatures (Figure D1(d), Figure D1(e)). The normalized current profile of the device without TiO_2 films in response to the external optical spike is shown in Figure D1(f). Its profile decay time is ∼0.04 s, which is much faster than that with TiO_2 films. As the pulse width increases from 0.05 s to 2 s, its current values only increase from ∼60 to ∼80 pA and the decay time retains within ∼0.04 s, the accumulation of which is much worse than that with TiO_2 layer at 260 °C in the current work. The EPR measurement is implemented for the TiO_2 layer to further prove the existence of oxygen vacancies in the TiO_2 layer (Figure D1(g)).

This finding further illustrated the modulation of the oxygen vacancies in the TiO_2 films on the decay behaviors of the synaptic devices. However, to understand clearly how the decay behavior is controlled by the defects call for study of determining the trapping energy levels. This determining of the trapping energy levels needs to combine the experimental method such as the deep level transient spectroscopy and the theoretic angle based on the molecular dynamic simulation in the future work.

Appendix E Device properties

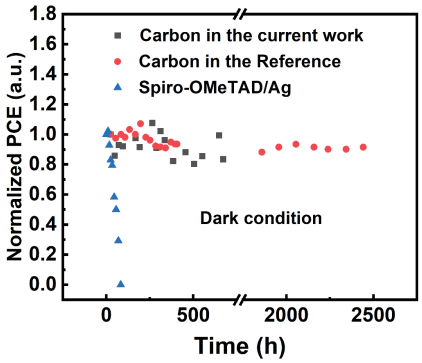

Figure E1 The storage stability data comparison for carbon and Ag electrodes in the dark condition.

The storage stability of the normalized PCE for the devices in N_2 atmosphere is shown in Figure E1. The black represented the devices with carbon (The device with TiO_2 layer annealed at 500°C as an example) from the current work while red represented the work from the reference [11]. The change tendency of the device with carbon from the current work was consistent with that from the reference.

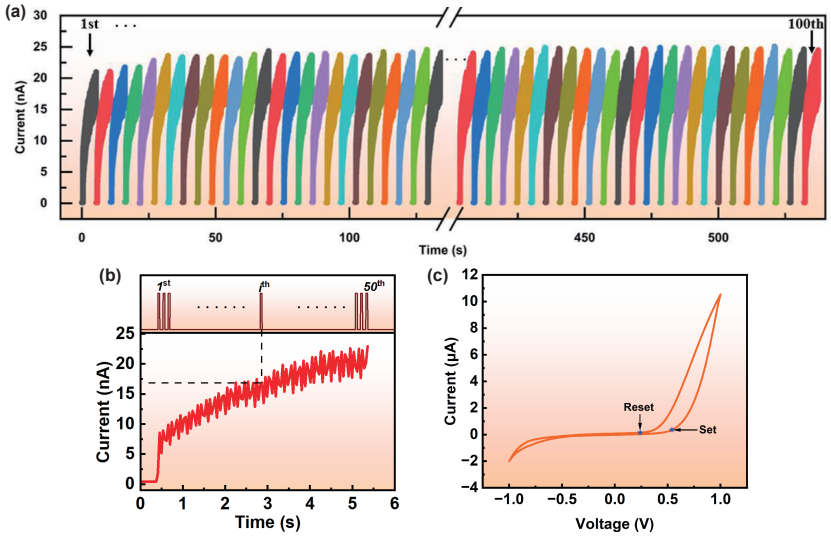

Figure E2 (a)Cycle-to-cycle variation of the SNDP behavior. (b)Synaptic response of the device in the i^{th} pulse.(c)$I-V$ curve for the set and reset points.

The cycle-to-cycle behaviors of the device based on the SNDP synaptic function is shown in Figure E2(a). The final consistency property (device-to-device and cycle-to-cycle) was obtained by averaging the variation coefficients at each pulse (Figure E2(b)). Meanwhile, the cycle-to-cycle variation is also evaluated by analyzing the set/reset voltages of the $I-V$ curves (Figure E2(e)). It is found that the variations for set/reset voltages are ∼6%/14%, respectively (Table E1). This is comparable to that of the cycle-to-cycle variation from the optical stimulation.

It should be noted that although the energy consumption density of the current system is larger than that in the work of Pi et al. [5], its variation and stability properties demonstrate better performance than that in the work of Pi et al. as shown in the Table E2. In addition, the current system obviously exhibits smaller device-to-device variation compared to that of the reference [12] even though the variation properties are based on the SNDP response at N=50 pulses, which is larger than that at N=5 [12]. More information about the performances of these devices is clearly demonstrated in Table E2. These results illustrate that the current device with carbon demonstrates superior comprehensive properties to the other reported self-powered synaptic devices in terms of energy consumption density, cost, and consistency and stability.

Table E1 Set and reset voltages for different cycles.

Voltage	1st	2ed	3rd	4th	5th	6th	7th	8th	9th	10th	Mean value	Standard deviation
SET (V)	0.64	0.60	0.58	0.58	0.56	0.56	0.54	0.54	0.54	0.54	0.57	0.03
RESET (V)	0.34	0.28	0.26	0.26	0.26	0.22	0.26	0.22	0.24	0.22	0.26	0.04

Table E2 Comparation of property parameters based on different self-powered optoelectronic synaptic devices. D means device-to-device. C indicates cycle-to-cycle; S is storage; O represents operational; '-' means there is no report, probably due to the poor performance of the corresponding parameters in these devices.

Device	Power(μ W/cm^2)	Width(s)	Energy Density(nJ/cm^2)	SNDP-D-Variation/ C-Variation ($N > 1$)	S/O Stability	Ref.
FTO/TiO_2/$MAPbI_3$/Carbon	41	0.05	2.05×103	∼10%/∼6.7%	672 h/720 h	This work
ITO/PCBM/$MAPbI_3$:Si NCs/Spiro-OMeTAD/Au	10	0.05	0.5×10^3	-/-	-/-	[12]
ITO/SnO_2/Al_2O_3/$CsBi_3I_{10}$/Au	100	1	1×10^5	-/-	-/-	[13]
ITO/$Cs_3Bi_2Br_9$/PMMA/Ag	35500	0.1	3.55×10^7	-/-	-/-	[14]
ITO/$CsPbBr_2I$/P3HT/Ag/ SiNx/n-Si/p-Si/Al	60000	1	0.4×10^7	-/-	-/-	[15]
ITO/$CsPbBr_2I$/P3HT/Au/ ITO/Au/Spiro-OMeTAD/ $CsFAPbI_3$/SnO_2/ITO	100000	0.2	2×10^7	-/-	-/-	[16]
ITO/$Cs_2AgBiBr_6$/P(VDF-TrFE)/Au	36.6	0.1	3.66×10^3	∼16%/∼7.5%	1344 h/-	[17]
Au/PMMA/C8-BTBT/F_{16}CuPc/Au	30000	0.05	1.5×10^6	-/-	-/-	[18]
PET/Au/PBTT/PMMA	10000	0.5	5×10^6	-/-	720 h/0.5 h	[19]
Au/C8-BTBT(PMMA)/Ag	10000	0.2	2×10^6	∼19%/-	-/-	[20]

References

1 Zhou H, Shi Y, Dong Q, et al.Hole-conductor-free, metal-electrode-free TiO_2/$MAPbI_3$ heterojunction solar cells based on a low-temperature carbon electrode. J. Phys. Chem. Lett., 2014,5: 3241-3246.
2 Chen H N, Yang S H. Methods and strategies for achieving high-performance carbon-based perovskite solar cells without hole transport materials. J. Mater. Chem. A, 2019,7: 15476-15490.
3 Snook J H, Samuelson L A, Kumar J, et al. Ultraviolet photoelectron spectroscopy of nanocrystalline TiO_2 films sensitized with $\left(2,2^{'}-\text{bipyridyl}\right)$ ruthenium(II) dyes for photovoltaic applications. Org. Electron., 2005,6: 55-64.
4 Mei A, Li X, Liu L, Ku Z, et al. A hole-conductor-free, fully printable mesoscopic perovskite solar cell with high stability. Science, 2014,345: 295-298.
5 Huang W, Hang P J, Wang Y, et al. Zero-power optoelectronic synaptic devices. Nano Energy, 2020, 73: 104790.
6 Jackman S L, Regehr W G. The mechanisms and functions of synaptic facilitation. Neuron, 2017,94: 447-464.
7 Lee G M, Scott L. Muscle response to changing neuronal input in the lobster (panulirusinterruptus) stomatogastric system: spike number versus spike. frequency-dependent domains. J. Neurosci., 1997,17: 5956-5971.
8 Larry F A, Wade G R. Synaptic computation. Nature, 2004,431: 796-803.
9 Clive R B. LTP $\neq$ learning: lessons from short-term plasticity. Front. Behav. Neurosci., 2010,4: 3.
10 Bejaoui B, Updates on titanium dioxide. IntechOpen, London, 2023.
11 Zhou H, Shi Y, Dong Q, et al.Hole-conductor-free, metal-electrode-free TiO_2/$MAPbI_3$ heterojunction solar cells based on a low-temperature carbon electrode. J. Phys. Chem. Lett., 2014,5: 3241-3246.
12 Lao J, Yan M, Tian B, et al. Ultralow-power machine vision with self-powered sensor reservoir. Adv. Sci., 2022,9: 2106092.
13 Hao D, Yang D, Liang H, et al. Lead-free perovskites-based photonic synaptic devices with zero electric energy consumption. Sci. China Inf. Sci., 2023,67:162401.
14 Zhao P, Cui M, Li Y, et al. Self-powered optoelectronic artificial synapses based on a lead-free perovskite film for artificial visual perception systems. J. Mater. Chem. C, 2023,11: 6212-6219.
15 Yang X, Xiong Z, Chen Y, et al. A self-powered artificial retina perception system for image preprocessing based on photovoltaic devices and memristive arrays. Nano Energy, 2020,78, 105246.
16 Ren Y, Bu X, Wang M, et al.Synaptic plasticity in self-powered artificial striate cortex for binocular orientation selectivity. Nat. Commun., 2022,13: 5585.
17 Lao J, Yan M, Tian B, et al.Ultralow-power machine vision with self-powered sensor reservoir. Adv. Sci., 2022,9: 2106092.
18 Hao Z, Wang H, Jiang S,et al. Retina-inspired self-powered artificial optoelectronic synapses with selective detection in organic asymmetric heterojunctions. Adv. Sci., 2022,9: 2103494.
19 Chen H, Lv L, Wei Y N, et al. Self-powered flexible artificial synapse for near-infrared light detection. Cell Rep. Phys. Sci.,2021,2:100507.
20 Jiang S, Peng L, Hao Z, et al. Self-powered organic optoelectronic synapses with binarized weights for noise-suppressed visual perception and high-robustness inference. ACS Appl. Electron. Mater., 2023,5: 4915-4924.